POLITECNICO DI TORINO
Repository ISTITUZIONALE

Sustainable multifunctional 3D printable eutectogels from biomass polymers for transient electronics and self-powered wearable devices

Original
Sustainable multifunctional 3D printable eutectogels from biomass polymers for transient electronics and self-powered wearable devices / Mogli, G., Martellone, S., Rolando, G., Villata, S., Lamberti, A., Ferrero, F., Frascella, F., Sorieul, M., Chen, Y.i., Stassi, S.. - In: CHEMICAL ENGINEERING JOURNAL. - ISSN 1385-8947. - 549:(2026), pp. 1-14. [10.1016/j.cej.2026.183212]

Availability:
This version is available at: 11583/3017198 since: 2026-10-29T12:02:37Z

Publisher:
Elsevier

Published
DOI:10.1016/j.cej.2026.183212

Terms of use:

This article is made available under terms and conditions as specified in the corresponding bibliographic description in the repository

Publisher copyright

(Article begins on next page)

20 November 2026

Chemical Engineering Journal 549 (2026) 183212

Contents lists available at ScienceDirect

Chemical Engineering Journal

journal homepage: www.elsevier.com/locate/cej

Sustainable multifunctional 3D printable eutectogels from biomass polymers for transient electronics and self-powered wearable devices

Giorgio Mogli [a], Simone Martellone [a,b], Gabriele Rolando [c], Simona Villata [a], Andrea Lamberti [a,b], Francesco Ferrero [c], Francesca Frascella [a], Mathias Sorieul [d], Yi Chen [d], Stefano Stassi [a,*]

[a] Politecnico di Torino, Dipartimento di Scienza Applicata e Tecnologia (DISAT), Corso Duca degli Abruzzi, 24, 10129, Torino, Italy
[b] Istituto Italiano di Tecnologia, Center for Sustainable Future Technologies, Corso Trento, 21, 10129, Torino, Italy
[c] Department of Agricultural, Forest and Food Sciences (DISAFA), University of Torino, Largo Braccini 2, 10095, Grugliasco, Italy
[d] Bioeconomy Science Institute, Titokorangi Drive, Private Bag 3020, Rotorua, 3046, New Zealand

ARTICLE INFO

Keywords:
Multifunctional eutectogel
Wearable sensors
3D printing
Sustainable Materials
self-powered sensor
Soil biodegradability

ABSTRACT

The rapid expansion of interconnected electronic systems poses increasing challenges to environmental sustainability, motivating the development of functional materials that combine high performance with end-of-life degradability. Here, we report a class of multifunctional eutectogels derived from biomass polymers, designed as versatile materials for sustainable transient electronics. These materials exhibit a unique combination of mechanical robustness, high flexibility, and long-term electrical stability, maintaining performance over three months under ambient conditions. The eutectogels display intrinsic antifreezing behaviour down to −50 °C and excellent skin compatibility, while undergoing visual soil degradation within seven weeks, demonstrating their suitability for environmentally benign applications. Their inherent ionic conductivity enables multimodal sensing capabilities, including strain sensing with a gauge factor of 1.6 and a detection limit of 0.06%, as well as reliable temperature and humidity monitoring. The materials are fully compatible with 3D printing techniques, enabling precise control over device architecture, mechanical compliance, and pressure-sensing performance. Beyond sensing, the eutectogels function as low-impact solid electrolytes in flexible supercapacitors, supporting stable operation over more than 5.000 charge–discharge cycles and enabling supercapacitor-integrated self-powered wearable systems. The combination of functional versatility and favourable environmental performance in a hypothetic industrial-scale life-cycle assessment (LCA) positions these eutectogels as promising material platform for next-generation sustainable transient electronics.

1. Introduction

Wearable electronic systems increasingly aim to emulate the sensory and adaptability of biological tissues, driving rapid advances in soft sensors capable of robust mechanotransduction at the human-device interface [1]. Unlike conventional rigid electronics, these systems must function under continuous deformation while maintaining stable electrical performance. Hydrogels, water-rich polymer networks, have emerged as a promising materials for wearable mechanosensors due to their intrinsic softness, tuneable mechanical and electrical properties, and biocompatibility [2]. By coupling mechanical deformation to electronic or ionic signal generation, hydrogel-based devices provide a materials-level route to mimic biological mechanotransduction. However, their long-term operational deployment as wearable remains limited due to environmental instability, particularly dehydration and freezing [3].

To address these limitations, alternative soft material systems in which water is replaced by low-volatility solvents, have attracted increasing attention as mechanically compliant yet environmentally stable sensing platforms [4,5]. Among them, eutectogels incorporating deep eutectic solvents (DESs) into soft polymeric networks exhibit high flexibility, long-term durability and sustained ionic conductivity, positioning them as promising candidates for robust soft sensors [6]. DESs typically comprise mixtures of hydrogen bond acceptors (commonly quaternary ammonium salts) and hydrogen bond donors (e.g., polyols, amines or carboxylic acids). Extensive hydrogen-bonding interactions

* Corresponding author.
E-mail address: stefano.stassi@polito.it (S. Stassi).

https://doi.org/10.1016/j.cej.2026.183212
Received 18 June 2026; Received in revised form 14 October 2026; Accepted 16 October 2026
Available online 19 October 2026
1385-8947/© 2026 The Authors. Published by Elsevier B.V. This is an open access article under the CC BY license (http://creativecommons.org/licenses/by/4.0/).

between these components induces a pronounced freezing-point depression of the individual constituents, enabling stable operation over a broad temperature range [7,8].

Despite these advances, most durable soft sensors still rely on polymer networks synthesized from petrochemical origin, owing to their favourable mechano-electric performance [9,10]. In contrast, biopolymers such as gelatin, cellulose and lignin offer intrinsic advantages including renewability, low toxicity and biodegradability, features that are becoming increasingly important amid growing concerns over electronic waste. Global e-waste generation is projected to reach 82 million tons by 2030, a nearly 32% increase from 2022, while recycling rates remain near 22% [11,12]. Beyond economic considerations, the release of hazardous substances from discarded electronics poses significant environmental risks [13], emphasizing the need for alternative sustainable materials strategies. Biopolymers thus represent a promising route towards transient or environmentally benign sensing devices [14–16]. Gelatin-based eutectogels have already been explored in literature, representing promising candidates for developing biocompatible, stretchable, highly sensitive and degradable strain sensors [17–19]. However, achieving a simultaneous combination of mechanical compliance, electrical conductivity and long-term stability in natural polymer-based systems remains, therefore limiting their adoption in mainstream flexible electronics [20].

Additive manufacturing has emerged as an enabling strategy for soft electronics, providing precise control over material architecture and tuning of mechanical compliance while enhancing sensing performance in conductive gel-like materials [21,22]. In parallel, the development of next-generation soft electronic devices increasingly calls for early-stage evaluation of environmental impact. Life cycle assessment (LCA) provides a standardized framework to quantify such impacts but remains underutilized in emerging electronics technologies [23,24]. Integrating prospective LCA at the design stage can reveal critical environmental trade-offs and guide the scalable development of soft electronic systems with minimized long-term impact.

Here, to address the lack of a material capable of simultaneously achieving multiple features desirable for flexible sensors, we report an ionically conductive, soft, and visually soil-degradable eutectogel entirely derived from abundant biomass feedstocks. Methacryloyl fish gelatin (GelMA) and cellulose nanofibrils (CNFs) sourced from brown algae were integrated within a deep eutectic solvent composed of choline chloride and glycerol to form a wholly natural-derived polymer network, cured via UV photopolymerization. The resulting eutectogel functions as a piezoresistive strain sensor with stretchability up to 140%, a gauge factor of 1.6 across the entire strain range, and a strain detection limit of 0.06%, together with low hysteresis and excellent repeatability. The eutectic solvent confers anti-freezing and anti-desiccation properties, maintaining stable mechanical and electrical performance for over three months, even at −45 °C. Incorporation of natural fillers (e.g., calcium lignosulphonate and tannins) enables mechanical properties fine tuning and high-fidelity 3D printing via digital light processing (DLP) process, yielding architected structures with enhanced pressure sensitivity. The printed GelMA–CNFs eutectogels undergo visual degradation in active soil within seven weeks, while cradle-to-gate LCA confirms substantially lower environmental impacts compared with petrochemical-based flexible sensors in a simulated industrial scenario. Biocompatibility tests on bio-fabricated 3D in vitro human epidermis models reveal no detectable skin irritation after 48 h of contact. Furthermore, this eutectogel serves as efficient gel electrolytes for flexible supercapacitors based on laser-induced graphene, enabling integrated self-powered sensing systems functioning up to 5000 charge-discharge cycles. Together, these results establish GelMA–CNF eutectogels as a sustainable, multifunctional material for next-generation wearable and transient electronics.

2. Results

2.1. Resin optimization

To develop a soft and ionically conductive eutectogel focusing on sustainability, biopolymers sourced from renewable biomass and biowaste streams were selected as primary feedstocks. Fish gelatine, a biomass-derived product obtained from fish-skin, is an inexpensive and environmentally friendly biopolymer, with tuneable physicochemical properties and a lower gelation temperature than porcine gelatine, enabling room-temperature processability [25]. Gelatin was methacrylated following a published protocol [26] to obtain photopolymerizable methacryloyl fish gelatine (GelMA) with a degree of functionalization (DoF) of 67.81 ± 3.77%. The effective functionalization was confirmed by FTIR analysis (Fig. S1). This GelMA was capable to form covalently crosslinked networks upon UV exposure. Cellulose nanofibrils (CNFs), high-aspect-ratio nanoscale fibres rich in hydroxyl groups, were incorporated as a soft entangled network reinforcing the mechanical properties of the GelMA matrix [27]. The CNFs were obtained as a byproduct of *Ecklonia Radiata*, a fast-growing algae species used as a fermentation substrate for biostimulant production. This secondary valorization pathway enables efficient resource use within marine biomass processing. The CNFs are produced through an eco-friendly pulping process, providing a rapidly renewable alternative to conventional wood-derived cellulose reinforcing their relevance for sustainable flexible electronics applications.

Gels with varying CNFs and GelMA contents, along with formulations incorporating different fillers, were systematically investigated. GelMA and CNFs aqueous suspension were mixed in a deep eutectic solvent composed of choline chloride (ChCl) and glycerol, yielding eutectogels, in which DES serves as the main liquid phase. A GelMA hydrogel (GelMA12water) was considered as reference. Complete compositions and nomenclature are reported in the Supporting Information (Table S1, S2). The addition of a hydrophilic and biocompatible photoinitiator lithium phenyl-2,4,6-trimethylbenzoylphosphinate (LAP) enabled UV-curing, resulting in the formation of a double network structure composed by a GelMA covalently crosslinked network and a CNFs entangled soft network (Fig. 1a).

The need for high-boiling-point solvents, like DESs, was motivated by the rapid water evaporation observed in conventional hydrogels under ambient conditions. As reported in Fig. 1b, GelMA12water hydrogel lost almost all its water within one month, leading to unstable mechanical and electrical performances. By contrast, DES-based eutectogel GDES12 exhibited only 7.74% average monthly weight loss, primarily attributable to initial unbound glycerol leaching. Incorporation of a small amount of CNFs aqueous suspension (GDES12_CNF03), further reduced water loss, likely due to the hydrogen bonding between the hydroxyl-rich CNFs and polymer-liquid phases [28]. However, increasing CNFs aqueous suspension loading (GDES12_CNF05), while enhancing elasticity, also increased overall water content and unbound water molecules, resulting in greater water loss. Increasing GelMA concentration mitigated this effect, yielded exceptionally stable eutectogels, with GDES20_CNF05 exhibiting only 2.34% weight loss after 30 days. The stark stability difference between hydrogel and eutectogel is visually evident in Fig. 1c, where the GelMA12water sample appears fully desiccated after one month. Differential scanning calorimetry (Fig. 1d) further confirmed the superior stability of both the pure eutectogel (GDES12) and the hybrid GDES20_CNF05 gel (containing DES and residual water from CNF suspension). Neither eutectogels exhibited freezing or melting transitions, unlike the hydrogel, demonstrating the exceptional thermal stability imparted by the glycerol-choline chloride DES across wide temperature ranges above and below 0 °C.

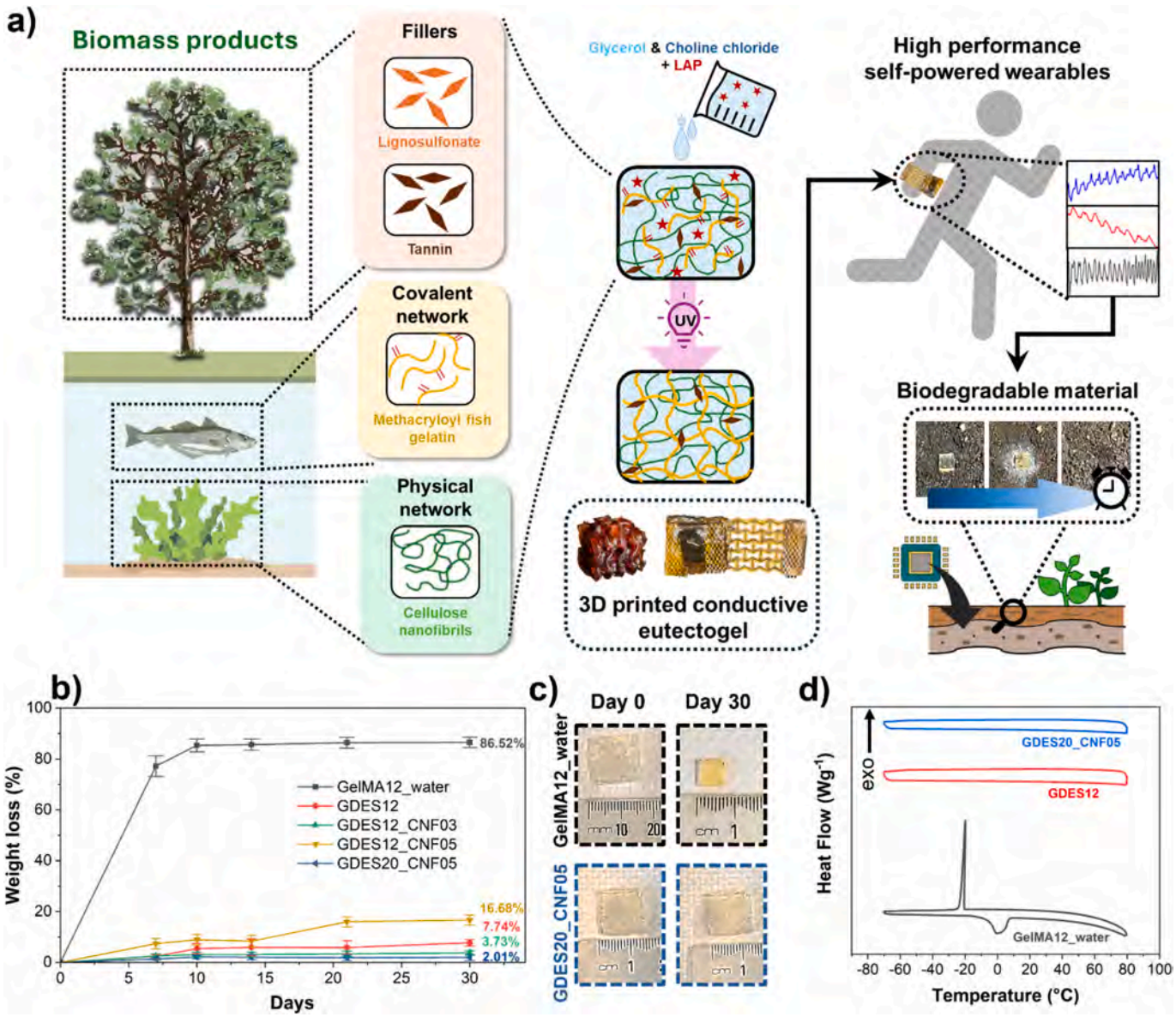


Fig. 1. Production and stability properties of the eutectogel based on biomass-derived polymers a) Schematic illustration of the manufacturing process of GelMA-CNF eutectogel sensors, from biomass-derived raw materials to visual soil degradation at end of life. b) Weight loss of parallelepiped-shaped samples of different gel types kept for 30 days under environmental conditions. Six independent samples were tested per formulation. c) Photographs of hydrogel and eutectogel sample as prepared (day 0) and after the testing period (day 30). d) Differential scanning calorimetry (DSC) of GelMA hydrogel (GelMA12_water), GelMA eutectogel (GDES12) and GelMA-CNF eutectogel (GDES20_CNF05).

2.2. Mechanical and electrical characterization

Once photopolymerized, GelMA-based eutectogels produced flexible and bendable materials (Fig. S2a). The CNF-free eutectogel (GDES12) showed limited elongation (57%) and brittle tensile behaviour (Fig. 2a). Incorporation of CNFs significantly improved stretchability and toughness, with GDES12_CNF05 achieving almost double elongation at break (~ 106%) and a 2.5-fold greater energy absorption capacity. This enhancement is ascribed, at least in part, to reversible hydrogen bonds between hydroxyl-rich CNF surface, water, the GelMA network and glycerol which can contribute to dissipate mechanical energy under external deformations [29]. This is consistent with FTIR spectra of GDES12 and GDES12_CNF05 samples (Fig. S2b), which exhibited a shift of O-H/N-H and Amide *I* band towards lower wavenumber (Fig. S2b). Similar behaviour was observed in GDES12 and GDES12_CNF05 samples after overnight drying (30 °C. under vacuum), indicating that these changes cannot be solely attributed to the presence of water. Overall, these investigations suggest that the incorporation of both CNFs and associated water contributes to a reorganization of the hydrogen-bonding network within the GelMA matrix [30,31]. However, excessive CNFs loading (GDES12_CNF1), introduced additional water, diluting the polymer and solvent contents and compromising mechanical performance.

Using GDES12_CNF05 as a baseline, GelMA concentration was then increased from 12 to 30 wt% relative to the DES. As shown in Fig. 2b, higher GelMA contents resulted in stiffer eutectogels with reduced elongation, consistent with the formation of a denser covalent GelMA networks, while toughness was enhanced, yielding materials with reduced brittleness (Fig. 2c). The formation of an insoluble crosslinked polymer network was further supported by gel fraction analysis in water, yielding 11.73 ± 1.05% residual mass after extraction of unreacted and soluble fractions from the photopolymerized samples, closely matching the theoretical GelMA+CNFs solid fraction of 11.44% (Fig. S2c). From this analysis, GDES20_CNF05 was selected as

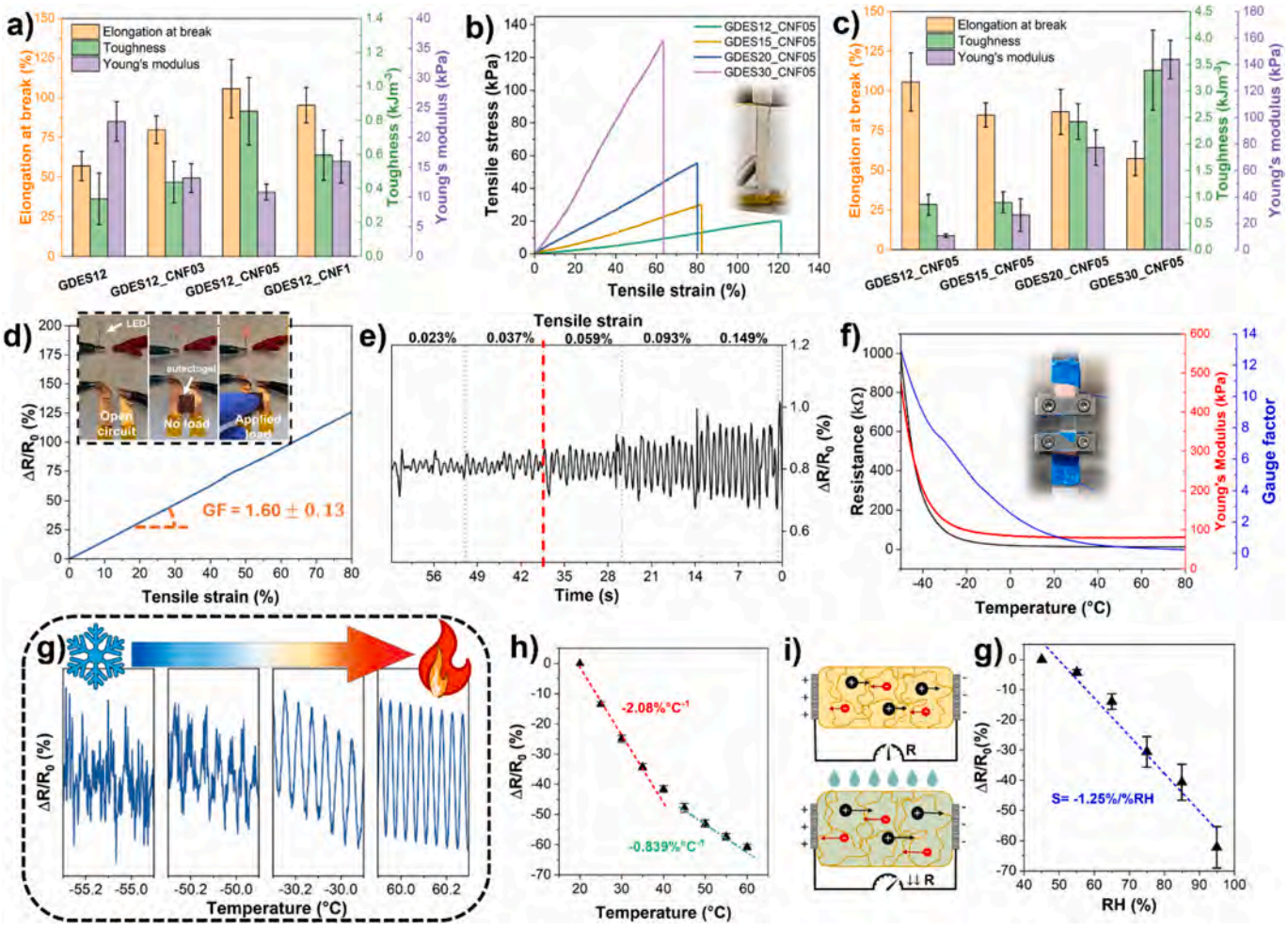


Fig. 2. Mechanical and multifunctional sensing properties a) Mechanical properties of gels with different CNF concentrations. Five independent dumbbell-shaped samples were test for each material. b) Stress-strain curves of eutectogels with varying GelMA concentrations under tensile test. In the inset the optical image of a GDES12_CNF05 sample under tensile stretching. c) Mechanical properties of gels varying GelMA concentrations. Five independent dumbbell-shaped samples were test for each material. d) Piezoresistive transfer curve of GDES20_CNF05. Gauge factor (GF) across the entire strain range is reported. In the inset, image of the electrical setup where the eutectogel is used to close the circuit enabling the LED connected in series to turn on. The LED brightness varies under different loads on the sensor due to changes in electrical eutectogel resistance. e) Resistance signal of GDES20_CNF05 sample subjected to small cyclic tensile strains (1 Hz). Higher tensile strains are reported in Fig. S3a. f) Electrical resistance, Young's modulus and strain sensitivity dependency on temperature of GDES20_CNF05 sample under DMTA test. g) Relative resistance variations of GDES20_CNF05 sample, during the DMTA testing under cyclic tensile loading (1% strain, 1 Hz), zoomed in four different temperature ranges. h) GDES20_CNF05 resistance behaviour under different temperatures, referred to resistance measured at 20 °C. Sensitivities to temperature are reported nearby for the two observed linear ranges. Five independent strip samples were tested. i) Illustration of the humidity sensing mechanism for the ionically conductive eutectogel. g) Resistance values of GDES20_CNF05 samples to different relative humidity values. Resistance variations compared to the resistance measured at 40%RH are reported. Linear fit is represented through the red dashed line. Sensitivity value is reported nearby. A pool of three independent samples was tested.

representative formulation, balancing relatively high stretchability (86%), good toughness and a stiffness of 80 kPa, mechanically compliant to soft biological tissues [32].

Thanks to the mobile ions from choline chloride, the GelMA-CNFs eutectogels exhibited ionic conductivity. Connecting the eutectogel in series with a LED across a potential difference (scheme in Fig. S2d) successfully illuminated a LED, with brightness increasing under eutectogel compression, owing to its reduced electrical resistance (inset of Fig. 2d). This deformation-induced electrical resistance changes, due to the extension or compression of ions conductive pathway between electrodes, known as piezoresistive effect, positions this conductive soft material as promising flexible strain sensors (Fig. 2d). The resistance variations-strain curve of GDES20_CNF05 was linear across the whole strain range, with an average gauge factor (GF) of 1.6. Under 100 cyclic tensile tests at 30% strain, the eutectogel exhibited low mechanical hysteresis (<8%) (Fig. S2e), optimal strain recovery (~89%) (Fig. S2f) resulting in a minor resistance signal drift (Fig. S2g). Significantly, the resistance amplitude (Δ_{cycles}), remain consistent across all cycles, confirming repeatable sensing performance.

Small strain sensitivity was assessed using dynamic mechanical thermal analysis (DMTA). Cyclic resistance response matched applied strains (Fig. S3a), even being clearly resolved down to 0.059% strain (Fig. 2e). Below this value, the electrical noise, visible as unstable resistance fluctuation, dominated. Indeed, strain sensitivity remained constant above this threshold, defining it as lower limit of detection (Fig. S3b). Moreover, the sensor exhibited rapid response and recovery times (~500 ms) (Fig. S4a), and stable operation both at low- and high-frequencies input up to 2 Hz (Fig. S4b,c), resulting suitable to capture both slow and fast deformations.

DESs are well-known for imparting thermal stability to polymeric materials [33], preventing water molecules crystallization through extensive hydrogen bonding at subzero temperatures [34]. Resistance

response of eutectogel was then evaluated under cyclic tensile stimuli while varying the temperature from −60 to +80 °C (Fig. 2f), revealing strong temperature dependence. At subzero temperatures the low ionic mobility increased the resistance and noise, while high temperatures led to exponential resistance decay and reduced strain sensitivity (blue curve, Fig. 2f). This reduction is primarily caused by the eutectogel softening, demonstrated by decreasing Young's modulus (Fig. S5a, logarithmic scale), resulting in reduced strain-induced perturbation of the conductive pathways for ions [35]. However, strain sensing remained reliable down to −50 °C (Fig. 2g) demonstrating the anti-freezing capabilities of GDES20_CNF05 eutectogel. The temperature dependence of resistance was further investigated by electrochemical impedance spectroscopy (Fig. S5b) which confirmed the increase in ionic conductivity with rising temperature (Fig. S5c).

Therefore, when properly calibrated, the GDES20_CNF05 eutectogels can monitor external temperature variations (Fig. 2h). The sensor displayed two linear regions, the first one ranging from 20 to 40 °C, with a negative temperature coefficient (NTC) of 2.08%°C^{-1}, the second, up to 60 °C, with a NTC of 0.839%°C^{-1}. In addition, response to rapid temperature change from 25 to 35 °C (performed in 12 s) led to a decrease in resistance stabilized after ~80 s (Fig. S5d). Cooling back to 25 °C, performed at the same rate, saw the resistance returned to its original value after ~45 s (Fig. S5e). As expected for polymeric material, resistance variations induced by temperature occurs slower than those caused by mechanical deformations. Cyclic heating-cooling between 25 and 40 °C (180 s/cycle) showed good amplitude repeatability besides baseline resistance drift attributable to slow thermal equilibration of the system (Fig. S5f).

Humidity also affects eutectogel conductivity due to glycerol well-known hygroscopic nature [36]. Moisture uptake from ambient air increases water content within the eutectogel matrix reducing the viscosity of the liquid phase. Therefore, ions mobility is improved, thereby increasing electrical conductivity and consequently decreasing resistance of the material (Fig. 2i). The electrical resistance decreased by ~65% following a quasi-linear trend when measured across relative humidity (RH) levels from 45 to 95 RH% at a fixed temperature (25 °C) (Fig. 2g). Analysis of the negative transfer curve yielded an RH sensitivity of 1.25%RH^{-1}, showing the multi-functional sensing ability of the eutectogel towards humidity, mechanical deformation and temperatures.

2.3. 3D printed sensors performances

Material processability is critical, for enhancing sensing performance

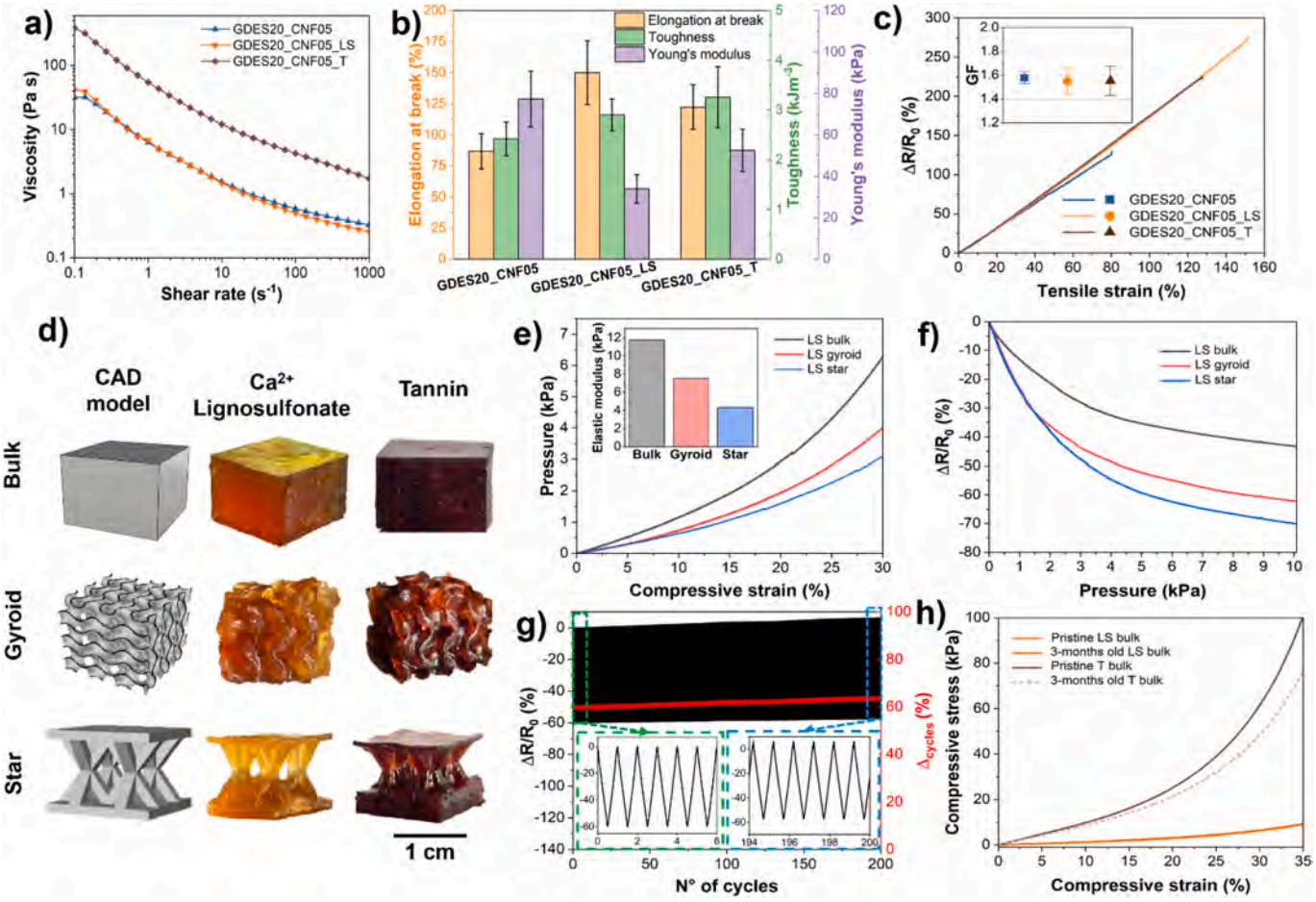


Fig. 3. 3D printed pressure sensors a) Rheological measurements of neat GDES20_CNF05 eutectogel and with different fillers. b) Tensile mechanical properties of GDES20_CNF05 with different fillers (Calcium lignosulfonate and tannin). Five independent dumbbell-shaped samples were test for each material. c) Piezoresistive transfer curves of neat eutectogel, lignosulfonate filled one and tannin filled one. In the inset, the average gauge factor across the entire strain range. Five independent samples were tested. d) Computer-Aided Design (CAD) models and the corresponding 3D printed objects fabricated using the lignosulfonate- and tannin-based inks. e) Compressive stress-strain behaviour of the 3D printed architectures with lignosulfonate filler. In the inset the compressive elastic moduli of the different printed architectures. f) Piezoresistive behaviour of the GDES20_CNF05_LS 3D printed structures under compressive stress testing. g) Cyclic compressive test (200 consecutive cycles) on *Star*-shaped eutectogel. On the right axis, the amplitude (Δ_{cycles}) of each cycle is reported. Insets show zoomed in view of representative cycles at the beginning and at the end of the test (same scale bars as the main graph). h) Stress strain curves of bulk structures containing lignosulfonate and tannin fillers, measured after 3 months and compared with the as made (pristine) samples.

and facilitating device integration into wearable systems and complex, non-planar surfaces. In this context particularly DLP 3D printing, offers a precise control over geometries and mechanical properties, enabling highly sensitive devices. Although the neat photopolymerizable eutectogel (GDES20_CNF05) is compatible with UV-assisted additive manufacturing, its high UV-sensitivity led to resin overcuring and limited print resolution (Fig. S6a). To address this drawback, calcium lignosulfonate (LS) and tannin (T), two widely available, renewable and biodegradable wood-derived products [37,38] with intrinsic UV-blocking properties, were introduced as upcycled fillers, significantly improving DLP printing fidelity as described in detail in the Supporting Information, showing deviations with respect to the CAD model mostly within the range of ±0.2 mm (Fig. S6g). Both fillers contain hydroxyl groups, able to interact with the polymeric network, influencing both ink rheology and mechanical properties of the printed samples. Rheological measures (Fig. 3a) revealed that tannins promote the formation of physical bonds within the polymeric matrix, increasing ink viscosity, whereas this effect is less pronounced in LS-based inks due to fewer interactions with the matrix, resulting in a lower viscosity resin that enables faster printing.

The incorporation of fillers also improved tensile mechanical properties of the eutectogel (Fig. S7a-b). Elongation at break was significantly improved, to ~122% and ~ 150% for LS- and T-filled eutectogels, respectively, accompanied by a toughness increase of ~20% and ~ 35% (Fig. 3b). Even at very low loading (0.2 wt%), these additive significantly alter the eutectogel structure by introducing reversible bonds that likely increase chains mobility, reducing overall stiffness while increasing stretchability [39] (Fig. 3b). Importantly, the strain-sensing performance of eutectogels were maintained, with a linear response and a gauge factor of 1.6 (Fig. 3c).

Given the excellent resolution of the fillers-containing inks, complex architectures with different voids densities were 3D printed using both lignosulfonate- and tannin-based formulation (Fig. 3d). Stiff *bulk* geometry, softer *gyroid* and *star* architectures were 3D printed for evaluating pressure-sensing performance (Fig. 3e). Under compressive loading, electrical resistance diminished due to shortening of ionic pathway between electrodes. LS-eutectogel *Star* architecture exhibited a higher-pressure sensitivity than the LS *bulk* (Fig. 3f), due to larger deformations and greater changes in ion path length under identical loads. Similar trends were observed for the tannin-based printed eutectogels (Fig. S8a-b), with a slightly lower sensitivity owing to the higher stiffness of the tannin-resin. These results show that, 3D printing offers not only a route to tailor device geometry for its intended function, but also a complementary way for tuning the mechanical and sensing properties of the sensors.

Printed *Star* samples exhibited excellent repeatability under 200 compressive cycles at (30% strain, Fig. S9a) with an average hysteresis of ~6% for both LS and T samples and a strain recovery superior to 70%, indicating a good elastic recovery after deformation (Fig. S9b,c) [40]. Piezoresistive response was stable in both samples, with minimal drift and a ~ 4% variation in the resistance cycles amplitude (Δ_{cycles}) (Fig. 4g, Fig. S9d). Long-term mechanical and electrical stability were further confirmed by minor variations in both mechanical behaviour (Fig. 4h), pressure-dependent resistance response (Fig. S9e) and electrical conductivity (inset of Fig. S9e) after three months of storage under ambient conditions.

2.4. Environmental impact and skin compatibility

When placed on a microorganisms-rich soil, the eutectogel visually degraded within a few weeks. To monitor degradation without interferences, 3D printed, parallelepiped-shaped eutectogels were positioned on an active soil surface under controlled environmental conditions and photographed weekly. After 1 week, shrinkage and fungal growth were evident (Fig. 5a). Between week 7 and 9, samples showed clearly evident degradation, without visible residues (Fig. S10), suggesting the potential for environmental degradation. Given the low environmental toxicity of the DES (choline chloride and glycerol) [41], and the natural-derived components (GelMA, CNF, lignosulfonate and tannin) [42–45], these eutectogels represent promising materials for environmental benign sensors, potentially addressing the e-waste concerns of conventional devices.

Beyond material performance, assessing the potential environmental impact of production is critical for emerging electronic technologies, where energy-intensive manufacturing and end-of-life sustainability pose major challenges [23]. Accordingly, a cradle-to-gate Life Cycle Assessment (LCA) was performed to compare this biomass-derived eutectogel sensor (GDES20_CNF05_LS) with a petrochemical-derived PVA/AAc/NaCl organohydrogel previously reported by our group [35], selected for its similar fabrication route and sensing performances. The carbon footprint of both sensors was evaluated at laboratory scale and under simulated industrial-scale scenario to estimate their potential environmental impact at commercial production level. The industrial-scale scenario was modelled following the methodology reported by Piccinino et al. [46] A cradle-to-gate LCA was conducted within the system boundaries illustrated in Fig. 5b, and the corresponding greenhouse gas (GHG) emissions are reported in Fig. 5c. At laboratory scale, the bio-based eutectogel sensor exhibited higher GHG, primarily due to the gelatine methacrylation step. However, under the simulated industrial-scale scenario, it showed approximately half the GHG emissions of the petrochemical counterpart (0.011 vs 0.025 kg CO_2 eq. per gram of sensor). At this scale, the dominant contribution arises from raw material production, particularly glycerol. Across the broader LCA analysis, the biomass-derived sensor exhibited lower impacts in 13 out of the 16 evaluated environmental indicators. Detailed LCA methodology and additional impact categories are provided in the Supplementary Information (Figs. S11, S12). Although the obtained results depend on the assumptions made, this early-stage evaluation allows the identification of the processes and materials contributing most significantly to the environmental impact of sensor production under a simulated industrial scenario. Beyond the quantitative results, the comparison of similar gel materials for soft-sensor applications suggests that the choice of biomass-derived polymers could contribute to reducing the overall environmental impact, particularly in terms of CO_2 emissions. This highlights the potential of biomass-derived feedstocks as a promising strategy for developing more environmentally sustainable soft sensors, while further optimization and validation at larger production scales are needed. Furthermore, the sensitivity analysis supports the robustness of this environmental assessment under different industrial-scale production conditions, including different chemical reactor volumes (Table S17) and different 3D-printing facilities (Table S18).

Given its intended wearable use, eutectogel requires careful cytocompatibility assessment given its direct skin contact. Conventional in vitro evaluations models based on 2D monolayer cultures of keratinocytes or dermal fibroblasts fail to capture biochemical and biomechanical cues essential for in vivo-like cell proliferation, differentiation, and tissue organization [47]. By contrast in vitro 3D epidermal models better mimic stratified architecture and barrier function, providing realistic evaluation of irritation, cytotoxicity, or leachate-induced damage from flexible sensors [48]. Four weeks-cultured epidermis samples were analysed via LIVE/DEAD kit at 1, 6, 24 and 48 h after contact with GDES20_CNF05_LS and GDES20_CNF05_T 3D printed sensor (Fig. S13). Keratinocyte viability remained above 90% for both materials at all time points (Figs. 4d, S14; quantification in Fig. 4e), indicating no detectable cytotoxicity. Immunofluorescence analyses further confirmed epidermal barrier integrity, with consistent expression of pancytokeratin and filaggrin, indicating intact cytoskeletal organization and barrier function (Figs. 4f and Figs. S15, S16). Together, these results demonstrate that the eutectogel sensors neither compromise epidermal viability nor structural integrity, supporting their suitability topical wearable applications.

Combining excellent mechanical, physical, and multi-sensing

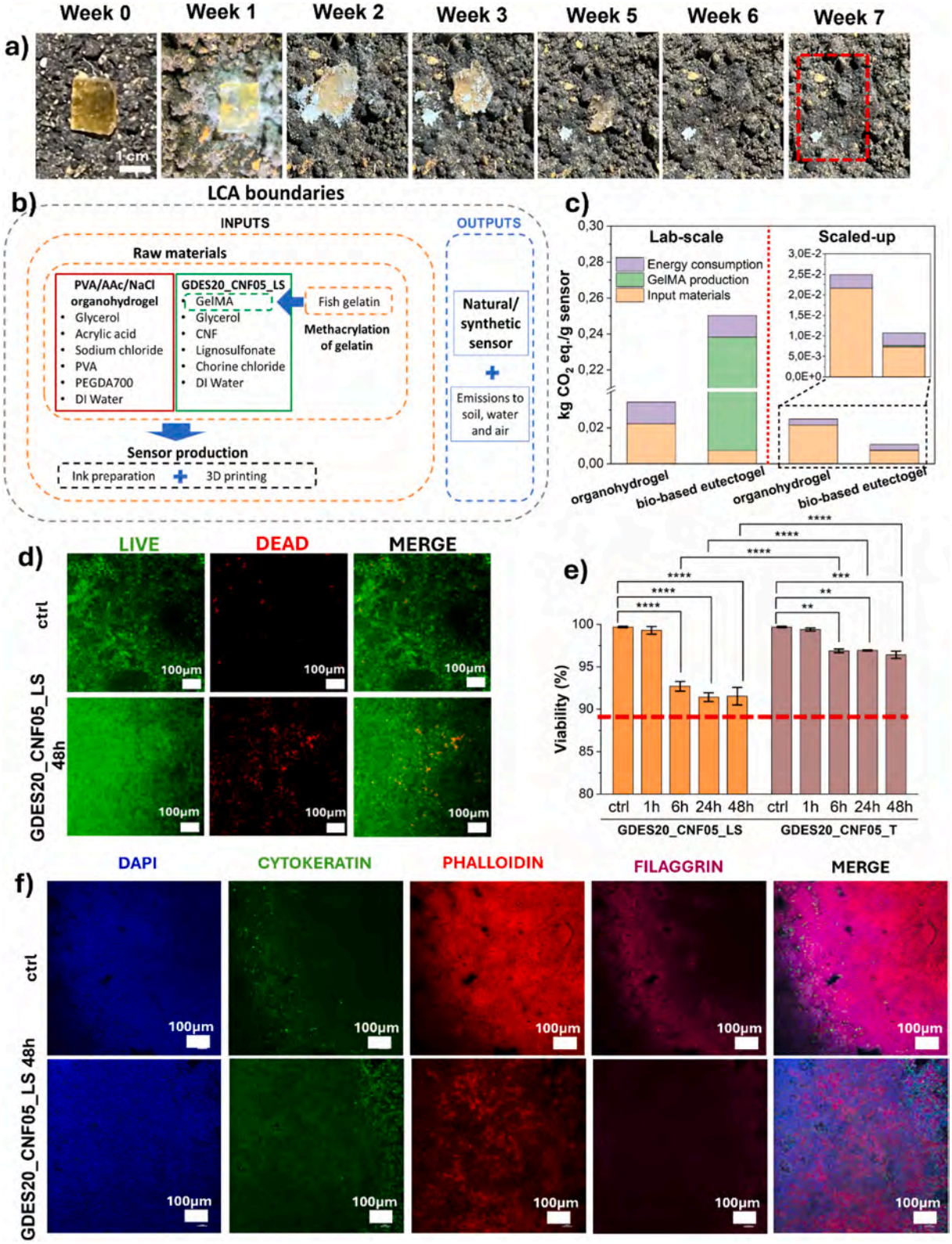


Fig. 4. Environmental impact and cytotoxicity analysis a) Visual soil degradation of GDES20_CNF05_LS sample over a period of seven weeks. b) System boundaries of the Life Cycle Assessment (LCA). c) Carbon footprint (CF) per gram of sensor for organohydrogel and bio-based eutectogel, evaluated at laboratory scale and under a simulated industrial production scenario. d) Fluorescent images of LIVE/DEAD assays on 3D in vitro epidermis model in contact with 3D printed GDE20_CNF05_LS for 48 h (down), respect to the control (up). The green channel shows alive cells while the red channel shows dead cells. Images are at 20× magnification. e) Quantification of cells viability starting from LIVE/DEAD analysis. Statistical analysis was performed using two-way ANOVA. *$p < 0.05$, **$p < 0.01$, ***$p < 0.001$, ****$p < 0.0001$. f) Immunofluorescence images of 3D in vitro epidermis model in contact with 3D printed GDE20_CNF05_LS for 48 h (down), respect to the control (up). DAPI was used to stain cellular nuclei (blue channel), TRITC-Phalloidin was used to stain the cytoskeletons (red channels), pancytokeratin is visualizable in FITC (green channel) while in Cy5 it is possible to observe filaggrin (magenta channel). Images are at 20× magnification.

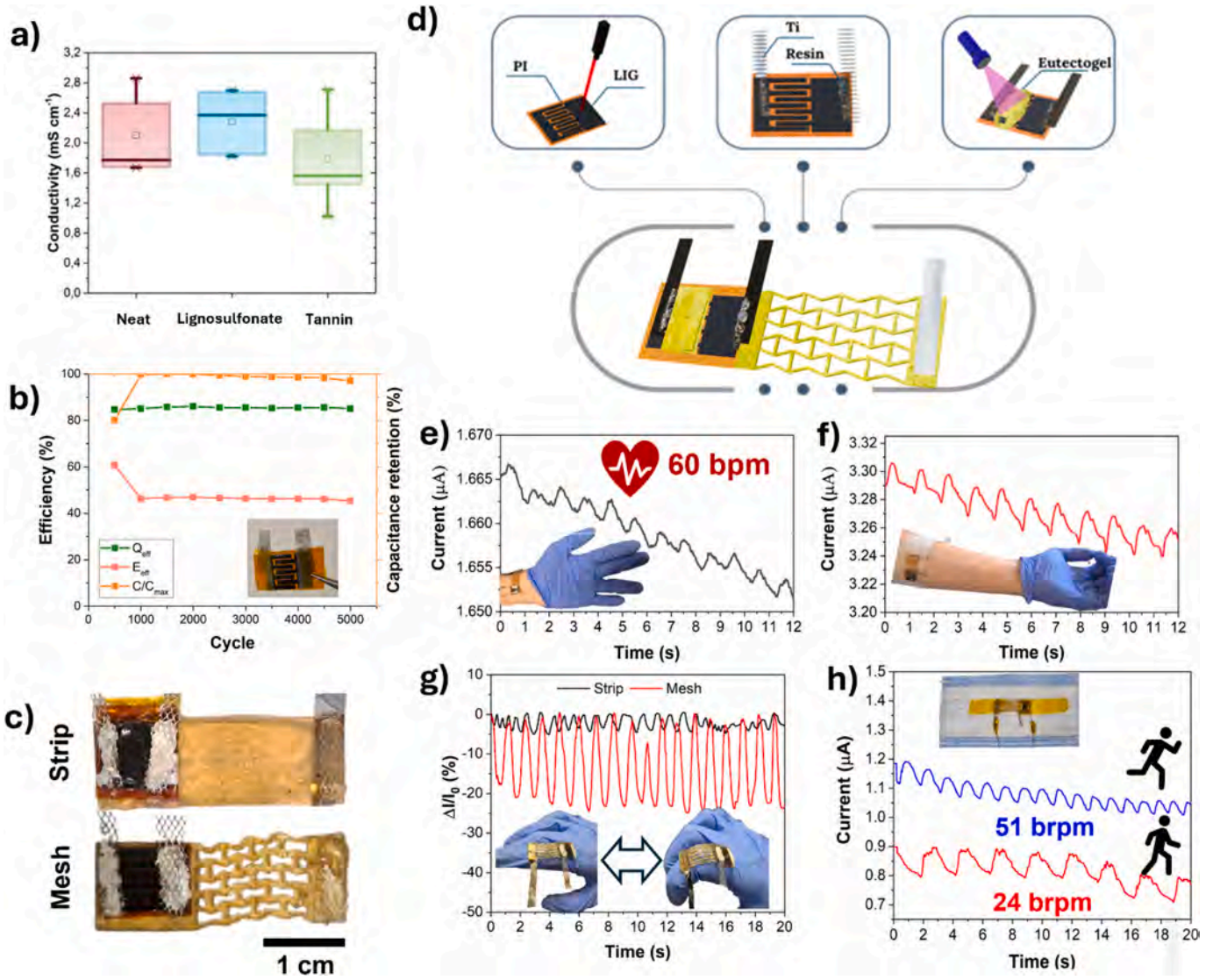


Fig. 5. Self-powered human biometric wearable sensors a) Conductivity of optimized 3D-printed eutectogels. b) Efficiency and capacitive retention over 5000 CCCD cycles for the calcium lignosulfonate supercapacitor (Inset: photo of energy storage device). c) Photos of integrated supercapacitor-sensor systems. d) Schematic of supercapacitor fabrication: CO_2 laser irradiation of PI substrate, titanium grid deposition for contacts/insulation with photocurable resin, eutectogel drop-casting with UV curing, and mesh sensor integration. e) Pulse wave at wrist and heartbeat monitoring. f) Extrinsic fingers muscles, placed on the forearm, activity detection during repetitive opening/closing of hand. g) Finger bending detection using strip or mesh geometries (data represented as relative to current variation from baseline). h) Breathing monitoring when the self-powered eutectogel sensor is applied at the inner part of a mask.

properties with rapid, reproducible 3D-printable fabrication, this skin-compatible and visually soil-degradable eutectogel emerges as one of the most versatile wearable sensors, including a comprehensive set of desirable features within a single material system based on polymers derived from biomass feedstocks, when benchmarked against literature counterparts (Table S4). Notably, among the compared systems, this work combines DLP-based fabrication with a polymer platform from biomass, providing the geometric freedom, higher resolution compared to direct-ink-writing technologies, and reproducibility of vat photopolymerization while retaining the sustainability advantages of bio-derived materials. In addition, the mechanical performance of the developed eutectogel is suitable for wearable strain-sensing applications, where the relevant deformation range is typically below 55% [49].

2.5. Self-powered sensing and applications

To enable autonomous operation in off-grid environments, a flexible and portable energy storage devices compatible with soft sensors are desirable. Planar, flexible supercapacitors represent a promising alternative to conventional bulky and rigid batteries, enabling an improved mechanical compliance and compact form factor [50]. The selection of the electrolyte is a fundamental step to design these devices. Gel electrolytes are particularly advantageous as they minimize solvent evaporation and simplify encapsulation [51]. Therefore, eutectogels were employed as supercapacitor electrolyte leveraging their intrinsic ionic conductivity provided by choline (Ch^+) and chloride (Cl^-) ions solvated within the glycerol and residual water solvent. All three eutectogels (GDES20_CNF05, GDES20_CNF05_LS, GDES20_CNF05_T) displayed sufficient ionic conductivity. However, while addition of tannin increased gel viscosity (Fig. 3a) reducing ions mobility and conductivity, calcium lignosulfonate introduced additional Ca^{2+} ions and sulfonate groups, resulting in slightly higher conductivity. This formulation was therefore selected as the most suitable electrolyte for the planar supercapacitor (Fig. 5a). Flexible supercapacitors were fabricated using interdigitated laser-induced graphene (LIG) electrodes [52], produced

by direct laser writing of a polyimide (PI) substrate. Inspired by the integrated architecture reported in our previous work [22], the present study introduces the biomass-derived eutectogel offering improved environmental profile and durability.

Electrochemical characterizations were performed to evaluate supercapacitors performance and stability (full experimental details are provided in the Supporting Information, Fig. S17). Constant current charge-discharge (CCCD) data (Fig. S17g) yielded areal energy and power density values of 1.8–4.8 nWh cm^{-2} and 0.8–14 μW cm^{-2}, respectively, sufficient for low-power sensing applications [53]. Furthermore, unlike conventional devices, this supercapacitor does not require encapsulation (e.g., pouch sealing) to prevent desiccation, as confirmed by 5000 charge/discharge cycles performed at 20 μA cm^{-2}, showing no performance degradation (Fig. 5b).

The planar supercapacitor was connected in series with the strain sensor to form a 3D printed, supercapacitor-integrated self-powered wearable device (Fig. 5c,d; full detail in Supporting Information Fig. S18). After charging the supercapacitor with an external power source, applied mechanical deformations modulated the discharge current through the eutectogel sensor (Fig. s18b,c). Under compression, the sensor resistance decreased (discharge current increased), whereas tensile strain increased resistance (current decreased). Upon load released, the current returned to baseline value. This mechanism enabled real-time monitoring of biomechanical signals (Fig. 5e-h), such as wrist pulse wave (Fig. 5e), fingers muscles activity during repetitive hand closure/opening (Fig. 5f), and finger bending (Fig. S19a,b). These measures were enabled by the intrinsic adhesivity of 3D printed GDES20_CNF05_LS to different substrates including nitrile-gloves, copper and glass (Fig. S20a), promoted by the different functional groups forming reversible bonds [18,54]. The eutectogel exhibited adhesive strengths ranging from 6 to 12 kPa (Fig. S20b), allowing the sensor to adhere to different materials without the usage of additional tape, including the irregular and deformable surfaces of human skin (Fig. S20c). Moreover, leveraging the design freedom provided by 3D printing, strip and mesh geometries were integrated with the supercapacitor (Fig. 5c). Under identical repeated finger-bending stimuli, mesh geometry produced larger current variations due to the improved conformability to curved surfaces and more efficient strain transfer (Fig. 5g), displaying the potential of 3D printing. Exploiting the eutectogel multi-sensing ability, the self-powered sensor was then fixed to the inner side of a mask to monitor breathing. In this confined environment, the sensor detected combined temperature and humidity changes associated with inspiration and exhalation cycles. As exhaled air is warmer and more humid than the ambient atmosphere, it caused a decrease in eutectogel resistance and a corresponding increase in current passing through the sensor (Fig. 5h). The breathing rate of a volunteer was then measured as 51 breath per min (brpm) while running decreasing to 24 brpm when the exercise intensity was reduced. The multi-stimuli sensitivity of this eutectogel represents both an advantage and a disadvantage, as different external stimuli provoke resistance change, resulting in potential cross-sensitivity preventing the independent quantification of the single stimulus. Future studies could address this problem through the integration of hardware strategies, such as encapsulations, reference sensors and tailored device architectures as well as software methods including signal processing or machine-learning techniques.

3. Conclusions

We present a multifunctional eutectogel composed of biomass-derived polymers, GelMA, CNFs, calcium lignosulfonate, and tannin. The resulting material exhibits optimal flexibility, 3-months durability, anti-freezing properties (down to −50 °C), and skin biocompatibility. Its ionic conductivity enables soft strain sensors (gauge factor = 1.6, minimum strain detectable = 0.06%), temperature and humidity sensing applications. The eutectogel 3D printability via DLP allows architectures structures that precisely tune mechanical and sensing properties. 3D-printed sensors were integrated with flexible supercapacitors using the same eutectogel as electrolyte, to fabricate portable, lightweight supercapacitor-integrated self-powered sensing systems, ideal for wearable applications. The monolithic integration of the supercapacitor and sensor, fabricated from the same material and sharing a common electrode, enables autonomous sensor operation after the energy-storage unit has been charged externally. Future integration of an energy-harvesting unit could replenish the stored energy during operation, thereby extending the device's autonomy and reducing its dependence on external charging. The exceptional versatility of this eutectogel based on biomass-derived polymers combined with its visual degradation in soil and favourable cradle-to-gate LCA under hypothetical scaled-up industrial scenario, positions it as promising platform for the next-generation of sustainable bio-electronics. Future investigations should extend the end-of-life assessment and LCA to the complete sensing system, including the electrodes, substrate, and potential encapsulation layers, to assess the feasibility of completely transient flexible devices.

4. Materials and methods

4.1. Materials

Gelatin from cold water fish skin, glycerol, choline chloride (≥ 98%), methacrylic anhydride, lithium phenyl-2,4,6-trimethylbenzoylphosphinate (LAP) were purchased from Sigma Aldrich (USA). Cellulose nanofibrils from *Ecklonia radiata* (CNF) were purchased from NanoSea (AgriSea, New Zealand). A 1 wt% CNF water solution was employed for this study. Calcium lignosulphonate was purchased from Borregaard (Norway). Pine bark tannins (from *Pinus radiata*), Mw 5000–7000, were kindly donated by the Biopolymer Network (New Zealand).

Cellular experiments were performed using human keratinocytes (HaCaT) purchased from Antibody Research Corporation and maintained in Gibco DMEM GlutaMAX high glucose, supplemented with 15% fetal bovine serum (FBS) (Sigma-Aldrich), 1% penicillin–streptomycin (Sigma-Aldrich), 1% L-glutamine (Sigma-Aldrich) and 1% sodium pyruvate (Sigma-Aldrich). For viability analysis, LIVE/DEAD cell assay kit (Sigma Aldrich) was used. For immunofluorescence, a pancytokeratin primary antibody (Novus Biologicals) and a filaggrin primary antibody (Invitrogen) were used. Anti-mouse 488 secondary antibody (Invitrogen) and anti-rabbit 647 secondary antibody (Invitrogen) were used to obtain the fluorescent signal. Alexa Fluor™ Plus 555 phalloidin (Invitrogen) was used for the cytoskeleton and DAPI (Sigma Aldrich) for the nuclei staining.

4.2. Photocurable inks preparation and eutectogels fabrication

A deep eutectic solvent was prepared by adding choline chloride to glycerol in a weight ratio of 1:2 respectively. The solution was magnetically stirred at 200 rpm and 50 °C until a transparent solution was achieved.

Methacryloyl gelatin (GelMA) was synthesized starting from fish gelatine, following the protocol reported by Loessner D. et al [26] Briefly, 20 g of fish gelatine were dissolved in 200 mL of deionized UltraPure water, stirring at 350 rpm and 55 °C until a homogeneous and clear solution is obtained (after roughly 45 min). Then, 12 g of methacrylic anhydride (MA), corresponding to 0.6 g of MA per 1 g of gelatine, was slowly added in 40 min to the gelatine solution under continuous vigorous stirring at 800 rpm and 50 °C. Then, the reaction solution was carried out for 2.5 h, maintaining the stirring velocity and temperature constant. Thereafter, the solution was centrifuged at 3500 *g* for 3 min, and the unreacted methacrylic anhydride collected at the bottom of the flask was eliminated. Then, 200 mL of deionized water at 40 °C was added to the supernatant and the resulting solution was dialyzed against deionized water at 40 °C for 7 days using 14-kDa membranes, with the water replaced daily. Following that, the pH of the dialyzed GelMA

solution was brought to 7.4 using 1 M $NaHCO_3$ aqueous solution and, at the end, it was freeze dried. The successful introduction of methacrylate groups onto fish gelatin was confirmed by FTIR-ATR analysis (Fig. S1).

For the eutectogels, freeze-dried GelMA was slowly added to the DES and stirred at 100 rpm and 50 °C, until a homogeneous solution, referred to as *GDESX*, where *X* stands for the weight percentage of GelMA relative to the DES, was achieved. Subsequently, a certain amount of CNF (1 wt% in water) was added to the preheated GDES solution, increasing the stirring velocity at 150 rpm. In the case of inks with tannin or Ca^{2+} lignosulfonate, the filler amount was inserted after the CNF, maintaining the same velocity and temperature (150 rpm, 50 °C). For the ink containing tannins, a further mechanical mixing using a homogenizer (IKA® ULTRA-TURRAX) was necessary to break up the tannins' agglomerates. In case of foam formation, the ink was placed in the vacuum oven at 40 °C until the air bubbles were completely removed.

For the water-based ink, GelMA was added to deionized water and stirred for 20 min at 150 rpm and 40 °C.

Once the temperature decreased to 30 °C, LAP photoinitiator was added to the inks with 1 wt% relative to the GelMA content and mixed at 150 rpm until fully dispersed.

The composition of all the photocurable inks investigated in this work are reported in Table S1.

The photocurable inks were poured in polydimethylsiloxane molds and exposed to UV lamp (OmniCure series 2000) equipped with a bandpass filter 320–480 nm for 4 min per side at a light intensity of 20 mW cm^{-2}. Dumbbell-shaped samples with 37 mm length, 12 mm width, 14 mm of gauge length, 3.8 mm gauge width and 1.5 mm thickness were fabricated for tensile test. Parallelepiped-shaped samples with nominal dimensions of 15x15x2 mm^3 were employed for compressive tests, durability assessment and degradation experiments. Strips of 12x6x2 mm^3 were produced for DMTA trials.

4.3. Degree of functionalization (DoF)

The degree of functionalization (DoF) of GelMA was evaluated by an o-phthalaldehyde (OPA) fluorescence assay based on the quantification of residual primary amine groups, as described elsewhere [55]. First, five different concentrations (0.02, 0.1, 0.5, 0.75 and 1 mg mL^{-1}) of unmodified fish gelatine were dissolved in Dulbecco's Phospated-Buffered Saline (DPBS) to derive the calibration curve. Fish GelMA control solutions (2 mg mL^{-1} in DPBS) was prepared. Then both the unmodified gelatine and GelMA formulations were reacted with OPA at a ratio of 1:2 *v/v*, and fluorescence intensity was read at 450 nm (excitation wavelenght = 360 nm) using a Synergy™ HTX Multi-Mode Microplate Reader (BioTek). The DoF was calculated according to Eq. (1):

$$DoF = \left(1 - C_{eq}/C_{sample}\right) \bullet 100 \quad (1)$$

where C_{eq} is the equivalent modified gelatin concentration of the sample determined by the calibration curve and C_{sample} is the effective GelMA sample concentration test (2 mg mL^{-1}). The experiment was conducted in triplicate.

4.4. Fourier-transform infrared spectroscopy

Fourier-transform infrared (FT-IR) spectroscopy was carried out in attenuated total reflectance (ATR) mode using a Nicolet iS50 FT-IR spectrometer equipped with a diamond crystal. Spectra were collected over the 4000–500 cm^{-1} range by averaging 32 scans at a resolution of 2.0 cm^{-1}.

4.5. Gravimetric analysis

Parallelepiped-shaped samples with the same nominal dimensions (15x15x2 mm^3) were stored in an unsealed Petri dish in a room at 25 °C and relative humidity 40%. The samples were periodically weighed over a period of one month, and the weight loss was computed relative to the initial conditions. Six samples were tested for each formulation.

4.6. Differential scanning calorimetry

Differential scanning calorimetry measures were carried out with a DSC 3 (METTLER Toledo) under nitrogen atmosphere. Samples, placed in aluminium crucibles, were first cooled at a rate of 10 °C min^{-1} down to −70 °C. Thereafter an isotherm of 15 min was performed. Subsequently a heating ramp at a rate of 10 °C min^{-1} up to 80 °C was carried out, followed by another isotherm of 15 min. The cycle was repeated twice in order to eliminate any effects related to the thermal history of the samples. The second cooling/heating cycle is reported.

4.7. Electrical measures and sensor performances

Electrical measures were performed through a LCR meter (HIOKI IM3536) to measure the electrical response of the sensor. An AC voltage of 0.5 *V* at 1 kHz was applied to measure the impedance that was modelled by a parallel capacitance (C_p) and a parallel resistance (R_p). The latter was considered to investigate the piezoresistive behaviour of the material. The choice of a frequency of 1 kHz derived from our previous study on a cellulose-based hydrogel [56].

The percentage relative resistance variations were then derived as follows:

$$\Delta R(t)/R_0(\%) = 100 \bullet (R(t) - R_0)/R_0 \quad (2)$$

where $R(t)$ represents the resistance measured at a certain time *t* of the test and R_0 is the resistance of the sample under rest conditions.

Sensitivity (*S*), also referred to as gauge factor (*GF*) in case of tensile tests, was computed in the linear region of the transfer curves using the following formula:

$$S = (\Delta R/R_0)/X \quad (3)$$

where $\Delta R/R_0$ is the relative variation of resistance within a certain stimulus range and *X* is the variation of the external stimulus applied.

4.8. Mechanical test

Tensile tests were performed up to rupture using a universal testing machine Instron (500 N as load cell) setting the crosshead velocity to 5 mm min^{-1}. Cyclic tensile tests were performed up to 30% of strain at a rate of 20 mm min^{-1} for 100 consecutive cycles. Copper foil sheets were used as electrodes.

An RSA-G2 solids analyzer (TA instruments) was used for compression test with a compressive speed of 0.5 mm min^{-1}. The same instrument was employed for compressive cyclic test performing 200 subsequent cycles at 30% of strain and a velocity of 20 mm min^{-1}. Copper sheets were placed in the top and bottom faces of the parallelepiped-shaped samples.

4.9. Dynamic mechanical thermal analysis (DMTA)

The RSA-G2 solids analyzer was employed for dynamo-mechanical thermal analysis (DMTA). A constant cyclic tensile strain of 1% at a frequency of 1 Hz were applied to strip samples, while temperature was varied from −60 °C to 80 °C with a rate of 3 °C min^{-1}. Resistance signal was acquired meanwhile. The percentual variations of each peak-valley resistance cycle were computed. By dividing the obtained values with the strain applied by the instrument (1% of strain), the curve of point-by-point sensitivity (Gauge factor) to tensile strain was derived.

The instrument was also utilized to investigate the minimum strain detectable by the eutectogel sensor. Cyclic tensile strains ranging from 6% down to 0.005%, decreasing in a logarithmic progression, were

applied at a constant frequency of 1 Hz at room temperature. Then, to assess the sensor sensitivity at different deformation rates, the tensile strain was kept constant at 1% changing the application frequency logarithmically from 0.05 Hz to 2 Hz. Also in this case, test was performed at room temperature. Strain sensitivity was derived by computing the relative resistance change for each loading cycle at different applied strain amplitudes. These values were then normalized by the corresponding applied strain, and sensitivity value was obtained under the assumption of a linear response. Average sensitivity values were calculated across multiple strain cycles.

Hysteresis degree was evaluated as:

$$\text{Hysteresis}\ (\%) = 100 \bullet \left(E_{loading} - E_{unloading}\right)/E_{loading} \quad (4)$$

where $E_{loading}$ is the loading energy, namely the area under the loading curve in the σ-ε graph and $E_{unloading}$ is the area under the unloading curve. In a cycle, the difference between the loading energy and unloading energy is the dissipated energy in that cycle.

Strain recovery was evaluated from cyclic tensile and compressive test according to:

$$\text{Strain recovery}\ (\%) = 100 \bullet (\varepsilon_{max} - \varepsilon_{residual})/\varepsilon_{max} \quad (5)$$

where ε_{max} is the maximum strain reached at the end of loading phase and $\varepsilon_{residual}$ is the residual strain measured at zero applied force during the unloading phase.

Adhesion performance was evaluated through a 180° peel test using a 50 N load cell. 3D printed specimens measuring 10 × 10 × 1.5 mm^3 were positioned between two substrates of the material being tested. The resulting assembly was subjected to a 300 g pressure for 5 min before testing. Adhesion was assessed on glass, nitrile and copper substrates; the latter two were previously bonded onto rigid glass supports. The peel test was performed at a constant displacement rate of 3 mm min^{-1}. The adhesive strength was determined as the ratio between the maximum force recorded during the test and the contact area.

4.10. Insoluble fraction analysis

The gel fraction of the photopolymerized samples was determined by solvent extraction in deionized water. The samples were initially weighed and kept in metal net and then immersed in DI water for 48 h at room temperature to extract the soluble and unreacted components. The samples were subsequently removed from the water and dried under vacuum at 40 °C for 10 h before weighing. The extraction procedure was then repeated for an additional 48 h, followed by a second drying step under vacuum at 40 °C for 10 h, with no significant variation in the measured mass. The gel fraction was calculated as the ratio between the final dry mass after extraction and the initial mass of the sample, expressed as a percentage.

4.11. Temperature sensing

Response to temperature variations was evaluated by clamping a strip sample in the tensile module of the RSA-G2 solids analyzer and then, keeping fixed the clamps, the chamber temperature was varied with a 5 °C degree step, from 25 °C to 60 °C. For each step, after waiting 5 min, sample's electrical resistance was measured for 1 min and average value was derived. Five independent samples were tested.

Responsiveness to temperature variations was evaluated by rapidly heating the chamber from 25 °C to 35 °C at a rate of 50 °C min^{-1}. Then the temperature was kept constant until the electrical resistance of the sensor reached stability. The same procedure was adopted for the cooling process.

Dynamic temperature measurement was carried out by heating and cooling the instrument chamber at a rate of *10 °C* min^{-1}, starting from 25 °C and reaching 40 °C, for four consecutive cycles. Electrical resistance was continuously measured during the test.

Percentage resistance variations and sensitivity were computed as previously described.

4.12. Humidity sensing

Eutectogel sensors were placed in a climatic chamber (Thermoline Australia temperature-humidity cabinet) and relative humidity (RH) was varied from 45% to 95% analysing sensors' response at every 10% increment. For each RH step, the humidity was kept constant for 15 min after which sensors resistance was recorded for 1 min and average value was computed. Temperature was kept constant at 25 °C.

Percentage resistance variations and sensitivity were computed as previously described. Experiments were performed in triplicate.

4.13. Rheology

Viscosity of the photoreactive inks was evaluated by a rheometer (Discovery HR-2, TA instruments) in parallel plate mode. A gap of 0.3 mm was set, and viscosities were evaluated at shear rates ranging from 0.1 to 1000 s^{-1}.

Reactivities to UV light were evaluated using a rheometer (Anton Paar Physica MCR 302) equipped with a photorheology module, operating in parallel plate mode (gap of 0.2 mm) and a quartz bottom plate. The UV light source was a Hamamatsu LC8 lamp with a central wavelength of 365 nm and an intensity of 20 mW cm^{-2}. Photorheology tests were carried out setting a constant strain amplitude of 1% and a constant shear frequency of 1 Hz to operate in the linear viscoelastic range.

4.14. 3D printing

The developed photocurable formulations were then employed as ink for a Digital Light Processing 3D printed (Asiga MAX X UV385) with 385 nm wavelength and a nominal resolution of 27 × 27 μm^2. The printing parameters are summarized in Table S2. After the printing process, unreacted resin was first removed through compressed air followed by immersion in ethanol and mild sonication for 30 *s*. Post curing was carried out for 5 min in a UV oven (Robofactory UV). Printing fidelity with respect to the original CAD models was investigated using a 3D optical scanner (E4, 3Shape, sensitivity 4 μm) by comparing the scanned objects with their corresponding reference model. The results are presented as coloured 3D map showinng the geometrical deviation from the original CAD design.

4.15. Degradation on soil

Parallelepiped-shaped samples with the same nominal dimensions (15 × 15 × 2 mm^3) and weighting approximately 500 mg each were placed on active soil in the dark at controlled humidity (RH ~ 90%) and temperature levels (~27 °C). Pictures were taken weekly, and degradation was visually evaluated. Triplicates of the studied eutectogels were monitored.

4.16. Life cycle assessment

An attributional LCA was conducted following the ISO 14040 and ISO 14044 standards (ISO, 2006a, 2006b). The goal of the study was to quantify the environmental impacts of eutectogel-based soft sensors. The considered functional unit (FU) was 1 g of sensor (both for GDES20_CNF05_LS and PVA/AAc/NaCl organohydrogel) produced at laboratory scale and at a hypothesized industrial production scenario. The system boundaries considered were from cradle-to-gate and the aspects of product use (i.e. product use, reuse and the end-of-life) of the products were not considered. The quantification of all inputs (e.g. raw materials, energy) from system boundaries were standardized according to functional unit. The environmental impacts were calculated through the ReCiPe 2016 v1.1 midpoint, Hierarchist perspective using SimaPro

9.6, through Ecoinvent v3.10, Agri-footprint v6.3 and U.S. Life Cycle Inventory (USLCI) databases. The stages of the LCA analysis and corresponding data and assumptions are described in detail in the "Life Cycle Assessment analysis" section at the end of the Supporting Information file.

4.17. 3D in vitro epidermis model

The epidermal model was biofabricated as previously reported [57]. In brief, HaCaT cells were seeded onto PET 12-well hanging inserts with a porosity of 0.4 μm (Milicell®) at a density of 2×10^5 cells/insert. The first three days of culture were performed as a submerged culture in complete Dulbecco's Modified Eagle's Medium (DMEM). Specifically, 1.5 mL of medium was used in the lower compartment and 1 mL in the upper compartment. This phase was necessary to facilitate the adhesion of keratinocytes to the insert membrane. After the first three days, air–liquid interface (ALI) culture commenced by supplying 500 μL of 3D-GRO™ Skin Differentiation Medium (Sigma) to the lower compartment while leaving the upper compartment in contact with air. The culture proceeded for a total of 5 weeks, with the medium changed every 2 days. Following epidermis maturation, 6 mm diameter, 1.5 mm thick sensors were placed on top of the epidermis model. Tests were performed using both lignosulfonate and tannin filled eutectogels. The models were analysed after 1, 6, 24 and 48 h to evaluate potential epidermal damage.

4.18. Live and dead

LIVE/DEAD cell assay kit (Sigma Aldrich) was used to evaluate cell viability after 1, 6, 24 and 48 h following sensor positioning. In detail, the 3D in vitro epidermal models were washed twice with DPBS, stained with 1.5 μM Propidium Iodide and 1 μM Calcein-AM for 30 min in an incubator at 37 °C and washed again with Dulbecco's Phosphate-Buffered Saline (DPBS) to remove the unreacted dyes. The fluorescence signals were detected using an Eclipse Ti2 Nikon (Tokyo, Japan) microscope equipped with a Crest X-Light spinning disk. For the quantification of cell viability, fluorescence images were processed using the Fiji/ImageJ software. Due to high cellular confluence hindering individual cell counting, a pixel-based area coverage analysis was performed. Briefly, the composite images were split into their respective green (live) and red (dead) channels. A global threshold was applied to each channel to generate binary masks representing the total area occupied by live and dead populations. The percentage of the field of view occupied by each signal was calculated using the *Area Fraction* parameter within the *Set Measurements* menu, ensuring the *Limit to Threshold* option was enabled. Cell viability was then expressed as the ratio of the area occupied by live cells (A_{live}) to the total area occupied by both live and dead cells ($A_{live} + A_{dead}$), according to the formula:

$$Viability\ (\%) = 100 \bullet A_{live}/(A_{live} + A_{dead}) \tag{6}$$

4.19. Immunofluorescence

3D in vitro epidermal models were stained after 1, 6, 24 and 48 h following sensor positioning. Specifically, the samples were fixed in 4% paraformaldehyde in DPBS (J61899.AK, Thermo Scientific) for 1 h at room temperature (RT). The fixed samples were then washed in DPBS, permeabilised with 0.25% Triton X-100 (Sigma-Aldrich) for 15 min, and blocked with a solution of 5% BSA (Sigma-Aldrich) and 0.1% Tween (Sigma-Aldrich) for 1 h.

For epidermal model analysis, two different antibodies were used at specific dilutions: pancytokeratin (2 μg/mL, Novus Biologicals) and filaggrin (10 μg/mL, Invitrogen). The primary antibodies were incubated overnight at 4 °C, after which the samples underwent three washes in DPBS supplemented with 0.1% Tween. The secondary antibody staining was then performed for 1 h at RT. Nuclei were stained with a solution containing 1 μM DAPI and 11 μM Alexa Fluor™ Plus 555 phalloidin (Invitrogen) in PBS for 30 min. Finally, the samples were analysed using an Eclipse Ti2 Nikon microscope (Tokyo, Japan) equipped with a Crest X-Light spinning disk confocal microscope.

Cellular cytoskeleton was stained with phalloidin (red channel) and the cellular nuclei with DAPI (blue channel). The cells were also stained with pancytokeratin (green channel) and filaggrin (magenta channel), epidermal markers involved in forming an organised, stable and functional barrier that can be impaired by contact with damaging materials. Pancytokeratin forms intermediate filaments essential for keratinocyte mechanical stability [58]. Filaggrin, is a key protein of the stratum corneum that contributes to barrier function, keratin filament aggregation, and formation of natural moisturizing factors [59].

4.20. Statistical analysis

Statistical analyses were performed using GraphPad Prism. Cell-viability experiments were conducted using three independently manufactured biological models for each experimental condition ($n = 3$ biological replicates). Data are presented as mean ± standard deviation (SD). The effects of material type and time point, as well as their interaction, were evaluated using two-way analysis of variance (two-way ANOVA), followed by Šídák's multiple-comparisons test. Statistical significance was defined as ($p < 0.05$). Significance levels are reported as follows: *($p < 0.05$), **($p < 0.01$), ***($p < 0.001$), and ****($p < 0.0001$).

4.21. Self-powered sensor

Laser-induced graphene (LIG) electrodes were fabricated using a CO_2 laser system (Colibrì-Laser Veronese, $\lambda = 10.6$ μm, $P_{max} = 10$ W, Italy) to graphenize 125 μm thick Kapton® sheets. The laser parameters were set to a power of 3 W, a scanning speed of 60 mm s^{-1}, and a pulse frequency of 1 kHz. The resulting electrodes were patterned into interdigitated structures with 4 fingers, and subsequently coated with 60 mg of ionogel, which served as the electrolyte. The ionogel was crosslinked after a few minutes. Each device had total dimensions of 10×12 mm^2. Electrical connections were established using two titanium grids to ensure reliable contact during characterization which are fixed by using silver paste and insulated with a photocurable resin.

Electrochemical measurements were performed using a multi-channel potentiostat (VMP3, Bio-Logic, USA) in a two-electrode configuration. The optimal operating voltage window was determined through cyclic voltammetry (CV) in the range 0–1.8 *V*, with a 0.1 *V* increment and a scan rate of 5 mV s^{-1}. Constant-current charge-discharge (CCCD) tests were conducted at 6, 12, 24, 48, and 120 μA by charging the device up to 0.4 *V* and discharging it to 0 *V*. From these data the discharge energy (E_d) and the relative power (P_d) have been evaluated as

$$E_d = \int_{T_d} i(t)V(t)\mathrm{d}t, P_d = \frac{E_d}{T_d} \tag{7}$$

where i(t) is the current, *V*(t) is the voltage and T_d is the discharging period. Specific quantities were calculated by dividing the computed quantities by the areal dimension of the supercapacitor (10×12 mm^2). The effect of scan rate on device performance was further investigated through CV measurements in the 0–0.4 *V* range at 1, 2, 5, 10, 50, 100, and 200 mV s^{-1}. Electrochemical impedance spectroscopy (EIS) measurements were performed at the open circuit potential (OCP) over a frequency range 1 MHz-10 mHz with 10 mV sinus amplitude. EIS was also employed to determine the high-frequency resistance (R_{hf}), which is used to calculate the ionic conductivity of the electrolytes. For this purpose, the eutectogels were placed between two parallel stainless-steel electrode plates, and the conductivity (σ) was calculated according to the equation:

$$\sigma = \frac{d}{R_{hf} A} \tag{8}$$

where d is the distance between the two electrodes and A is the gel's area. Five samples have been tested for each electrolyte composition. Additional CVs were recorded at 10 mV s^{-1}. within the 0–0.4 *V* range to assess the overall electrochemical behaviour of the microcapacitors.

CRediT authorship contribution statement

Giorgio Mogli: Writing – original draft, Methodology, Investigation, Formal analysis, Data curation. **Simone Martellone:** Writing – original draft, Methodology, Investigation, Data curation. **Gabriele Rolando:** Writing – original draft, Methodology, Investigation, Data curation. **Simona Villata:** Writing – original draft, Methodology, Investigation, Data curation. **Andrea Lamberti:** Writing – review & editing, Validation, Methodology, Conceptualization. **Francesco Ferrero:** Writing – review & editing, Validation, Conceptualization. **Francesca Frascella:** Writing – review & editing, Validation, Conceptualization. **Mathias Sorieul:** Writing – original draft, Investigation, Conceptualization. **Yi Chen:** Writing – review & editing, Supervision, Conceptualization. **Stefano Stassi:** Writing – review & editing, Validation, Supervision, Project administration, Conceptualization.

Ethics statement

The reported physiological measurements were limited to preliminary, non-invasive pilot demonstrations performed exclusively by the authors on themselves. No external participants were recruited, and no identifying or sensitive personal data were collected.

Declaration of competing interest

The authors declare that they have no known competing financial interests or personal relationships that could have appeared to influence the work reported in this paper.

Acknowledgements

This research was supported by the National Plan for Complementary Investments to the NRRP, project “D3-4Health - Digital Driven Diagnostics, prognostics and therapeutics for sustainable Health care” (project code: PNC0000001) and by the European Research Council (ERC) under the European Union's ERC Starting Grant agreement No. 949916 (project CO2CAP).

Appendix A. Supplementary data

Supplementary data to this article can be found online at https://doi.org/10.1016/j.cej.2026.183212.

Data availability

Data will be made available on request.

References

[1] Z. Chen, Y. Huang, B. Zhang, D. Sun, X. Yu, Deformable materials and structures in wearable haptic interfaces, Nat. Rev. Mater. (2026), https://doi.org/10.1038/s41578-025-00877-0.
[2] D. Song, X. Chen, M. Wang, Z. Wu, X. Xiao, 3D-printed flexible sensors for food monitoring, Chem. Eng. J. 474 (2023) 146011, https://doi.org/10.1016/j.cej.2023.146011.
[3] J.-Y. Yu, S.E. Moon, J.H. Kim, S.M. Kang, Ultrasensitive and Highly Stretchable Multiple-Crosslinked Ionic Hydrogel Sensors with Long-Term Stability, Nano-Micro Lett. 15 (2023) 51, https://doi.org/10.1007/s40820-023-01015-7.
[4] S. Li, et al., Eutectogel-based strain and temperature sensor with widely tunable mechanical properties regulated by copolymerization-induced phase separation and electrostatic interaction, Mater. Today Nano 25 (2024) 100440, https://doi.org/10.1016/j.mtnano.2023.100440.
[5] L. Jiang, et al., Flexible wearable sensors based on lignin doped organohydrogels with multi-functionalities, Chem. Eng. J. 430 (2022) 132653, https://doi.org/10.1016/j.cej.2021.132653.
[6] P.A. Mercadal, et al., Eutectogels: The multifaceted soft ionic materials of tomorrow, JACS Au 4 (2024) 3744–3758, https://doi.org/10.1021/jacsau.4c00677.
[7] Y. Zhang, Y. Wang, Y. Guan, Y. Zhang, Peptide-enhanced tough, resilient and adhesive eutectogels for highly reliable strain/pressure sensing under extreme conditions, Nat. Commun. 13 (2022) 6671, https://doi.org/10.1038/s41467-022-34522-z.
[8] K. Fan, et al., Highly stretchable, self-healing, and adhesive polymeric eutectogel enabled by hydrogen-bond networks for wearable strain sensor, Chem. Eng. J. 449 (2022) 137878, https://doi.org/10.1016/j.cej.2022.137878.
[9] T. Li, et al., Stretching-orientation reinforced double network solvent-free eutectic gels for ultrarobust, flexible human-machine interaction devices, Adv. Funct. Mater. 35 (2025) 2508233, https://doi.org/10.1002/adfm.202508233.
[10] X. Luo, et al., 3D printing of self-healing and degradable conductive ionoelastomers for customized flexible sensors, Chem. Eng. J. 483 (2024) 149330, https://doi.org/10.1016/j.cej.2024.149330.
[11] A. Kumar, M. Holuszko, D.C.R. Espinosa, E-waste: an overview on generation, collection, legislation and recycling practices, Resour. Conserv. Recycl. 122 (2017) 32–42, https://doi.org/10.1016/j.resconrec.2017.01.018.
[12] (UNITAR), U. N. I. F. T. A. R, The Global E-waste Monitors. https://ewastemonitor.info/global-e-waste-monitors, 2025.
[13] J. Lee, H. Choi, J. Kim, Environmental and economic impacts of e-waste recycling: A systematic review, Chem. Eng. J. 494 (2024) 152917, https://doi.org/10.1016/j.cej.2024.152917.
[14] M. Baumgartner, et al., Resilient yet entirely degradable gelatin-based biogels for soft robots and electronics, Nat. Mater. 19 (2020) 1102–1109, https://doi.org/10.1038/s41563-020-0699-3.
[15] W.B. Han, et al., Ultra-stretchable and biodegradable elastomers for soft, transient electronics, Nat. Commun. 14 (2023) 2263, https://doi.org/10.1038/s41467-023-38040-4.
[16] Q. Fu, Y. Chen, M. Sorieul, Wood-based flexible electronics, ACS Nano 14 (2020) 3528–3538, https://doi.org/10.1021/acsnano.9b09817.
[17] Y. Wang, Y. Jiang, S. Nechausov, A. Miriyev, IEEE 8th International Conference on Soft Robotics (RoboSoft), 2025, pp. 1–8.
[18] P.A. Mercadal, et al., Natural, biocompatible, and 3D-printable gelatin eutectogels reinforced with tannic acid-coated cellulose nanocrystals for sensitive strain sensors, ACS Applied Electronic Materials 5 (2023) 2184–2196, https://doi.org/10.1021/acsaelm.3c00075.
[19] M.L. Picchio, et al., Mixed Ionic and electronic conducting eutectogels for 3D-printable wearable sensors and bioelectrodes, Adv. Mater. Technol. 7 (2022) 2101680, https://doi.org/10.1002/admt.202101680.
[20] D. Gao, J. Lv, P.S. Lee, Natural polymer in soft electronics: opportunities, challenges, and future prospects, Adv. Mater. 34 (2022) 2105020, https://doi.org/10.1002/adma.202105020.
[21] Y. Rong, et al., Photocurable 3D printing gels with dual networks for high-sensitivity wearable sensors, Colloids Surf. A Physicochem. Eng. Asp. 659 (2023) 130828, https://doi.org/10.1016/j.colsurfa.2022.130828.
[22] G. Mogli, et al., Self-powered integrated tactile sensing system based on ultrastretchable, self-healing and 3D printable ionic conductive hydrogel, Adv. Funct. Mater. 34 (2023) 2307133, https://doi.org/10.1002/adfm.202307133.
[23] L. Teuerle, et al., Life-cycle assessment of printed electronic components - case study for organic electrochemical transistors, Adv. Electron. Mater. n/a (2025) e00372, https://doi.org/10.1002/aelm.202500372.
[24] S. Zhang, et al., Prospective life cycle assessment of a flexible all-organic battery, J. Clean. Prod. 373 (2022) 133804, https://doi.org/10.1016/j.jclepro.2022.133804.
[25] M. Longo, C. Francia, M. Sangermano, M. Hakkarainen, J. Amici, Methacrylated wood flour-reinforced gelatin-based gel polymer as green electrolytes for Li–O2 batteries, ACS Appl. Mater. Interfaces 16 (2024) 44033–44043, https://doi.org/10.1021/acsami.4c09073.
[26] D. Loessner, et al., Functionalization, preparation and use of cell-laden gelatin methacryloyl-based hydrogels as modular tissue culture platforms, Nat. Protoc. 11 (2016) 727–746, https://doi.org/10.1038/nprot.2016.037.
[27] Y. Deng, et al., Anisotropic cellulose nanofibril piezoionic organohydrogel fabricated by directional freezing for flexible strain sensors, Int. J. Biol. Macromol. 307 (2025) 142187, https://doi.org/10.1016/j.ijbiomac.2025.142187.
[28] Y. Ye, et al., Toughening hydrogels through a multiscale hydrogen bonding network enabled by saccharides for a bio-machine interface, Mater. Horiz. 12 (2025) 1878–1890, https://doi.org/10.1039/D4MH01645A.
[29] X. Hong, et al., Nanocellulose-reinforced conductive hydrogels with high stretchability and sensitivity, temperature, and pH multi-responsive properties for flexible wearable sensor devices, J. Appl. Polym. Sci. 142 (2025) e57254, https://doi.org/10.1002/app.57254.
[30] S. Carrasco-Saavedra, et al., Transient dual-response iontronic strain sensor based on gelatin and cellulose nanocrystals eutectogel nanocomposites, Adv. Mater. Interfaces 11 (2024) 2300536, https://doi.org/10.1002/admi.202300536.
[31] Z. Rao, et al., Genipin-crosslinked gelatin-based composite hydrogels reinforced with amino-functionalized microfibrillated cellulose, Int. J. Biol. Macromol. 222 (2022) 3155–3167, https://doi.org/10.1016/j.ijbiomac.2022.10.088.

[32] Y. Ohm, et al., An electrically conductive silver–polyacrylamide–alginate hydrogel composite for soft electronics, Nature Electronics 4 (2021) 185–192, https://doi.org/10.1038/s41928-021-00545-5.
[33] Z. Wei, et al., Environmentally tolerant multifunctional eutectogel for highly sensitive wearable sensors, Mater. Horiz. 12 (2025) 2604–2618, https://doi.org/10.1039/D4MH01665C.
[34] Z. Zhang, A. Yao, P. Raffa, Transparent, highly stretchable, self-healing, adhesive, freezing-tolerant, and swelling-resistant multifunctional hydrogels for underwater motion detection and information transmission, Adv. Funct. Mater. 34 (2024) 2407529, https://doi.org/10.1002/adfm.202407529.
[35] G. Mogli, I. Roppolo, A. Chiappone, S. Stassi, Multi-responsive 3D printable organohydrogel for the fabrication of durable and low-hysteresis flexible sensors, Appl. Mater. Today 44 (2025) 102675, https://doi.org/10.1016/j.apmt.2025.102675.
[36] J.W. Fluhr, R. Darlenski, C. Surber, Glycerol and the skin: holistic approach to its origin and functions, Br. J. Dermatol. 159 (2008) 23–34, https://doi.org/10.1111/j.1365-2133.2008.08643.x %J British Journal of Dermatology.
[37] R. Shorey, A. Salaghi, P. Fatehi, T.H. Mekonnen, Valorization of lignin for advanced material applications: a review, RSC Sustainability 2 (2024) 804–831, https://doi.org/10.1039/D3SU00401E.
[38] S. Molino, N.A. Casanova, J.Á. Rufián Henares, M.E. Fernandez Miyakawa, Natural Tannin Wood Extracts as a Potential Food Ingredient in the Food Industry, J. Agric. Food Chem. 68 (2020) 2836–2848, https://doi.org/10.1021/acs.jafc.9b00590.
[39] R. Núñez-Flores, et al., Physical and functional characterization of active fish gelatin films incorporated with lignin, Food Hydrocoll. 30 (2013) 163–172, https://doi.org/10.1016/j.foodhyd.2012.05.017.
[40] Z. Song, et al., Janus adhesion hydrogels with low hysteresis and high sensitivity toward precision flexible electronics underwater, Chem. Eng. J. 521 (2025) 166386, https://doi.org/10.1016/j.cej.2025.166386.
[41] L. Wei, et al., The application of deep eutectic solvents systems based on choline chloride in the preparation of biodegradable food packaging films, Trends Food Sci. Technol. 139 (2023) 104124, https://doi.org/10.1016/j.tifs.2023.104124.
[42] M. Ogonowski, et al., Multi-level toxicity assessment of engineered cellulose nanofibrils in Daphnia magna, Nanotoxicology 12 (2018) 509–521, https://doi.org/10.1080/17435390.2018.1464229.
[43] I.T. Tomasi, R.A.R. Boaventura, C.M.S. Botelho, Environmental impact assessment of tannin-based coagulants production from chestnut shells, J. Environ. Manag. 382 (2025) 125346, https://doi.org/10.1016/j.jenvman.2025.125346.
[44] G. Xu, X. Ding, M. Kuruppu, W. Zhou, W. Biswas, Research and application of non-traditional chemical stabilizers on bauxite residue (red sand) dust control, a review, Sci. Total Environ. 616-617 (2018) 1552–1565, https://doi.org/10.1016/j.scitotenv.2017.10.158.
[45] Y. Piao, et al., Biomedical applications of gelatin methacryloyl hydrogels, Engineered Regeneration 2 (2021) 47–56, https://doi.org/10.1016/j.engreg.2021.03.002.
[46] F. Piccinno, R. Hischier, S. Seeger, C. Som, From laboratory to industrial scale: a scale-up framework for chemical processes in life cycle assessment studies, J. Clean. Prod. 135 (2016) 1085–1097, https://doi.org/10.1016/j.jclepro.2016.06.164.
[47] M. Kapałczyńska, et al., 2D and 3D cell cultures – a comparison of different types of cancer cell cultures, Arch. Med. Sci. 14 (2018) 910–919, https://doi.org/10.5114/aoms.2016.63743.
[48] G. Mogli, S. Villata, A. Chiappone, F. Frascella, S. Stassi, 3D-printable biocompatible, self-adhesive and long-term stable organohydrogel for wearable sensors, Appl. Mater. Today 49 (2026) 103148, https://doi.org/10.1016/j.apmt.2026.103148.
[49] T. Yamada, et al., A stretchable carbon nanotube strain sensor for human-motion detection, Nat. Nanotechnol. 6 (2011) 296–301, https://doi.org/10.1038/nnano.2011.36.
[50] P. Zaccagnini, et al., Laser-induced graphenization of PDMS as flexible electrode for microsupercapacitors, Adv. Mater. Interfaces 8 (2021) 2101046, https://doi.org/10.1002/admi.202101046.
[51] H. Dai, et al., Polymer gel electrolytes for flexible supercapacitors: recent progress, challenges, and perspectives, Energy Storage Mater. 34 (2021) 320–355, https://doi.org/10.1016/j.ensm.2020.09.018.
[52] P. Zaccagnini, A. Lamberti, A perspective on laser-induced graphene for micro-supercapacitor application, Appl. Phys. Lett. 120 (2022), https://doi.org/10.1063/5.0078707.
[53] C. Shen, et al., A review of on-chip micro supercapacitors for integrated self-powering systems, J. Microelectromech. Syst. 26 (2017) 949–965, https://doi.org/10.1109/JMEMS.2017.2723018.
[54] Z. Qiao, et al., Environment-tolerant, inherently conductive and self-adhesive gelatin-based supramolecular eutectogel for flexible sensor, Int. J. Biol. Macromol. 282 (2024) 137219, https://doi.org/10.1016/j.ijbiomac.2024.137219.
[55] C.G. Gaglio, D. Baruffaldi, C.F. Pirri, L. Napione, F. Frascella, GelMA synthesis and sources comparison for 3D multimaterial bioprinting 12–2024 (2024), https://doi.org/10.3389/fbioe.2024.1383010.
[56] G. Mogli, A. Chiappone, A. Sacco, C.F. Pirri, S. Stassi, Ultrasensitive piezoresistive and piezocapacitive cellulose-based ionic hydrogels for wearable multifunctional sensing, ACS Appl. Electron. Mater. 5 (2023) 205–215, https://doi.org/10.1021/acsaelm.2c01279.
[57] S. Villata, et al., Broadly accessible 3D In vitro skin model as a comprehensive platform for antibacterial therapy screening, ACS Appl. Mater. Interfaces 16 (2024) 70284–70296, https://doi.org/10.1021/acsami.4c16397.
[58] N. Rahadiani, S. Sarwanti, D.R. Handjari, M. Stephanie, E. Krisnuhoni, Clinical implications of Cytokeratin 19 expression in patients with oral squamous cell carcinoma, Pathologica 115 (2023) 155–163, https://doi.org/10.32074/1591-951x-842.
[59] S. Kezic, I. Jakasa, Filaggrin and skin barrier function, Curr. Probl. Dermatol. 49 (2016) 1–7, https://doi.org/10.1159/000441539.